The Astrophysical Journal, 874:104 (9pp), 2019 March 20 https://doi.org/10.3847/1538-4357/ab07b9
© 2019. The American Astronomical Society. All rights reserved.

Widespread Molecular Outflows in the Infrared Dark Cloud G28.37+0.07: Indications of Orthogonal Outflow-filament Alignment

Shuo Kong[1], Héctor G. Arce[1], María José Maureira[1,2], Paola Caselli[2], Jonathan C. Tan[3,4], and Francesco Fontani[5]
[1] Dept. of Astronomy, Yale University, New Haven, Connecticut 06511, USA
[2] Max-Planck-Institute for Extraterrestrial Physics (MPE), Giessenbachstr. 1, D-85748 Garching, Germany
[3] Dept. of Space, Earth and Environment, Chalmers University of Technology, Gothenburg, Sweden
[4] Dept. of Astronomy, University of Virginia, Charlottesville, Virginia 22904, USA
[5] INAF—Osservatorio Astrofisico di Arcetri, L.go E. Fermi 5, I-50125, Florence, Italy
Received 2018 December 31; revised 2019 February 13; accepted 2019 February 15; published 2019 March 27

Abstract

We present ALMA CO(2-1) observations toward a massive infrared dark cloud G28.37+0.07. The ALMA data reveal numerous molecular (CO) outflows with a wide range of sizes throughout the cloud. Sixty-two 1.3 mm continuum cores were identified to be driving molecular outflows. We have determined the position angle in the plane-of-sky of 120 CO outflow lobes and studied their distribution. We find that the distribution of the plane-of-sky outflow position angles peaks at about 100°, corresponding to a concentration of outflows with an approximately east–west direction. For most outflows, we have been able to estimate the plane-of-sky angle between the outflow axis and the filament that harbors the protostar that powers the outflow. Statistical tests strongly indicate that the distribution of outflow-filament orientations is consistent with most outflow axes being mostly orthogonal to their parent filament in three dimensions. Such alignment may result from filament fragmentation or continuous mass transportation from the filament to the embedded protostellar core. The latter is suggested by recent numerical studies with moderately strong magnetic fields.

Key words: accretion, accretion disks – galaxies: star formation – ISM: jets and outflows – ISM: magnetic fields – stars: protostars – stars: statistics

1. Introduction

While it is generally accepted that low-mass stars ($M \lesssim 8\,M_{\odot}$) form in low-mass dense molecular cores (Shu et al. 1987), the formation of massive stars ($M \gtrsim 8\,M_{\odot}$) has been actively debated (Motte et al. 2018). One of the central questions in the study of massive star formation (SF) is how massive stars gain their mass (Tan et al. 2014). One group of theories extend the idea of low-mass SF and argue that massive SF begins with a massive prestellar core (see reviews in McKee & Ostriker 2007). During the past decade, surveys of massive prestellar cores using interferometry were able to find candidates with masses up to $\sim 30\,M_{\odot}$ (Duarte-Cabral et al. 2013; Wang et al. 2014; Kong et al. 2017, 2018b). However, other interferometric observations suggest that cores may not provide enough mass for massive SF (e.g., Sanhueza et al. 2017). Alternatively, the other group of theories emphasize the dominant role of clump-scale accretion (~10 times larger than a core) in determining the final stellar mass. In this case, massive SF begins with low-mass "seeds", and no massive cores are needed (see reviews in Zinnecker & Yorke 2007). In other words, in the first scenario, the mass supply for massive SF is initially contained in a small volume (core), while in the second scenario, the mass supply is from a much larger volume. Currently, both theories need to be tested by further observations.

Auditing the mass budget of massive SF is essential to understanding the origin of the stellar initial mass function (IMF). In particular, it helps to clarify whether the IMF originates from the so-called core mass function (CMF; Chabrier & Hennebelle 2010; Hopkins 2012). Filaments are ubiquitous inside star-forming clouds (André et al. 2014). One idea of filament-feeding SF was proposed based on line-of-sight observations of velocity gradients along filaments (Kirk et al. 2013; Peretto et al. 2014). The gradients were interpreted as mass flows along the long axis of filaments. The flows were believed to funnel additional mass supply to the SF "hub", providing one mechanism that potentially solves the aforementioned mass-deficit problem. However, as pointed out by Fernández-López et al. (2014), the interpretation of the flows in the Serpens South molecular cloud (Kirk et al. 2013) is subject to projection effects. Fernández-López et al. (2014) raised a few other possibilities that could also explain the velocity gradient along the filaments, casting doubts on the filament-feeding idea.

To observationally confirm that the filaments are indeed feeding SF, one needs to first seek evidence that the protostellar accretion and the host filament are correlated. It is difficult to directly image the accretion in cores due to the high resolution needed to trace the gas flow and the complexity of the gas kinematics at these scales. A common assumption is that protostellar jets launched by the rotating accretion disk of the protostar can be used to trace the angular momentum direction of the accretion disk (see Frank et al. 2014, and the references therein). Bipolar molecular outflows driven by protostellar jets are much easier to trace than accretion disks (Arce et al. 2007; Bally 2016). We can therefore compare the position angle between outflows and filaments, both easily observable in large-scale maps of clouds, to search for evidence of the accretion-filament correlation. For instance, if the outflow-filament orientation shows a preferred angle, we may confirm that filaments play an important role in the protostellar accretion, and possibly the final stellar mass.

Recently, Stephens et al. (2017, hereafter Stephens17) investigated the outflow-filament orientation in the Perseus molecular cloud. Based on a statistical analysis of 57 protostars, Stephens17 found that either the orientations of

outflows with respect to their natal filament is random, or they are composed of a mixture of parallel and perpendicular directions. The former may be a result of perturbation from turbulent accretion (Fielding et al. 2015; Offner et al. 2016). Yet, a recent numerical study by Li et al. (2018) showed that a mostly orthogonal outflow-filament orientation is possible in massive infrared dark clouds (IRDCs). Under the condition of moderately strong magnetic fields, Li et al. (2018) showed that filaments form perpendicular to the field and protostellar cores inside the filaments launch outflows that are perpendicular to the filaments. Thus far, no strong observational evidence has been found to support the alignment between outflows and filaments.

IRDC G28.37+0.07[6] (hereafter G28) is a massive ($10^5\,M_\odot$) IRDC at a distance of 5 kpc. The central region of the cloud is dark at up to 100 μm (Ragan et al. 2012), indicating an extremely early evolutionary stage of SF. The dark region creates strong absorption against the Galactic background at near and mid infrared wavelengths, allowing researchers to derive its column density through extinction mapping (reaching 0.7 g cm^{-2}, Butler et al. 2014) and investigate the column density probability distribution function (Lim et al. 2016). At (sub-)mm wavelengths, Wang et al. (2011), Zhang et al. (2015), Tan et al. (2016), and Kong et al. (2018b) studied localized dense cores and outflows. Interestingly, Wang et al. (2011) noticed a hint of outflow-filament alignment in the P1 clump in G28, and later, Wang et al. (2012) suggested a perpendicular magnetic field direction in the same region. Recently, Cosentino et al. (2018) found evidence of widespread SiO emission in G28, indicating prevalent protostellar activities in the cloud.

In this paper, we present new ALMA CO(2-1) mosaics that reveal widespread molecular outflows across the IRDC G28. Our new ALMA mosaics extend the area in G28 that was studied by the aforementioned papers and cover the majority of this IRDC. The high angular resolution and high sensitivity of the ALMA data show strong evidence that the outflow-filament orientation in G28 is preferentially orthogonal. The implications for the SF process, in particular the potential connection between filament and protostellar accretion, will be discussed.

2. ALMA Observations

The CO(2-1) data cube was obtained under the ALMA project 2015.1.00183.S (PI:Kong). It is an 86-pointing mosaic that covers the majority of the IRDC G28. Kong et al. (2018a) studied the 1.3 mm continuum detection under the same project. We refer the readers to that paper for details on the ALMA observations. The CO line data cube was cleaned using the `tclean` task in CASA 5.1. Briggs weighting with a robust number of 0.5 was used, resulting in a final synthesized beam of $0\farcs6 \times 0\farcs4$, providing a linear resolution of about 0.012 pc (the cloud is at a distance of 5.0 kpc). The maximum recoverable scale is $\sim 20''$ (corresponding to the shortest baseline of 10 kλ with λ being 1.3 mm), which is about 0.5 pc at the distance to G28. The final cube sensitivity, with 1.3 km s^{-1} wide velocity channels, is $\sim$2.5 mJy beam^{-1}, or 0.22 K. As will be introduced in Section 3.1, we also use SiO (5-4) data to help confirm CO outflows. The SiO data cube is from a joint de-convolution of the data from 2015.1.00183.S and the data from 2013.1.00183.S (PI:Kong), which has the same spectral set-up (but different uv-coverage). More detailed studies of the SiO outflows will be presented in a future paper.

[6] The name of "G28.37+0.07" is from the *MSX* IRDC catalog from Simon et al. (2006) and has been used by Schneider et al. (2015), Lim et al. (2016), and Kong et al. (2018a). However, Carey et al. (2000) originally used "G28.34 +0.06" and this name has been used by Pillai et al. (2006), Wang et al. (2008, 2011), and Zhang et al. (2009, 2015).

3. Analysis and Results

3.1. CO Outflow Definition

Figure 1 shows a false-color image of the CO outflows and continuum cores. The green color shows the 1.3 mm continuum emission. The blue color shows the blueshifted CO(2-1) integrated intensity, and the red color shows the redshifted CO(2-1) integrated intensity. The velocity ranges of integration are symmetric about the cloud centroid velocity of 79.3 km s^{-1}, which previous studies obtained by analyzing the spectral line data of dense gas tracers (Pillai et al. 2006; Tan et al. 2013; Kong et al. 2016).

We detect bipolar molecular outflows that are distributed throughout the IRDC. Several outflows are parsec-scale (possibly even larger as some of the largest outflows reach the limits of the ALMA mosaic), indicating that outflow feedback may inject turbulent energy at $\gtrsim$pc scale. Some outflows show evidence suggestive of precession. Some show possible evidence of interaction with other nearby outflows.

We visually identify bipolar red–blue pairs that are symmetric around mm continuum sources. To produce the best results, we made 10 pairs of velocity-range integrated intensity maps of the redshifted and blueshifted emission integrated over 6.5 km s^{-1} wide (5 channels) chunks, that are symmetric around the cloud centroid velocity of 79.3 km s^{-1}. The 10 blueshifted velocity-range integrated maps range from 11.7 to 75.4 km s^{-1}, while the redshifted ones range from 83.2 to 146.9 km s^{-1}. The rms noise for each 6.5 km s^{-1} wide integrated intensity map is 7.3 mJy beam^{-1} km s^{-1}, or equivalently 0.64 K km s^{-1}.

With each velocity-range pair, we made a false-color image similar to Figure 1 and used it to visually search for bipolar CO emission. Then, we assigned the continuum source at the center as the driving source. We started with the highest-velocity pair, which includes blueshifted emission from 11.7 to 16.9 km s^{-1} and redshifted emission from 141.7 to 146.9 km s^{-1}, because they only include high-velocity outflows and show little "contaminating" cloud emission. We subsequently inspect maps of lower velocity blue–red pairs and add any new outflows to our list. We then verify our outflow catalog by carefully inspecting the CO emission from each channel in the cube, particularly paying attention to high-velocity emission close to continuum sources to search for small outflows that might have not been clearly depicted in the velocity-range integrated intensity maps. In a few cases, we use the SiO(5-4) line data to help determine the axes of some of the CO outflows that have a more complex emission structure. We only include unipolar outflows in our list if we detect high-velocity blue or redshifted emission with a morphology that suggests that it is associated with a continuum source (e.g., if the continuum source is located at the narrow end of an elongated high-velocity structure).

The continuum sources in this region were identified and cataloged by Kong (2019, hereafter K19). In total, 280 cores were defined in K19 using their method. The numerical names of the cores follow the rank of 1.3 mm continuum flux. K19

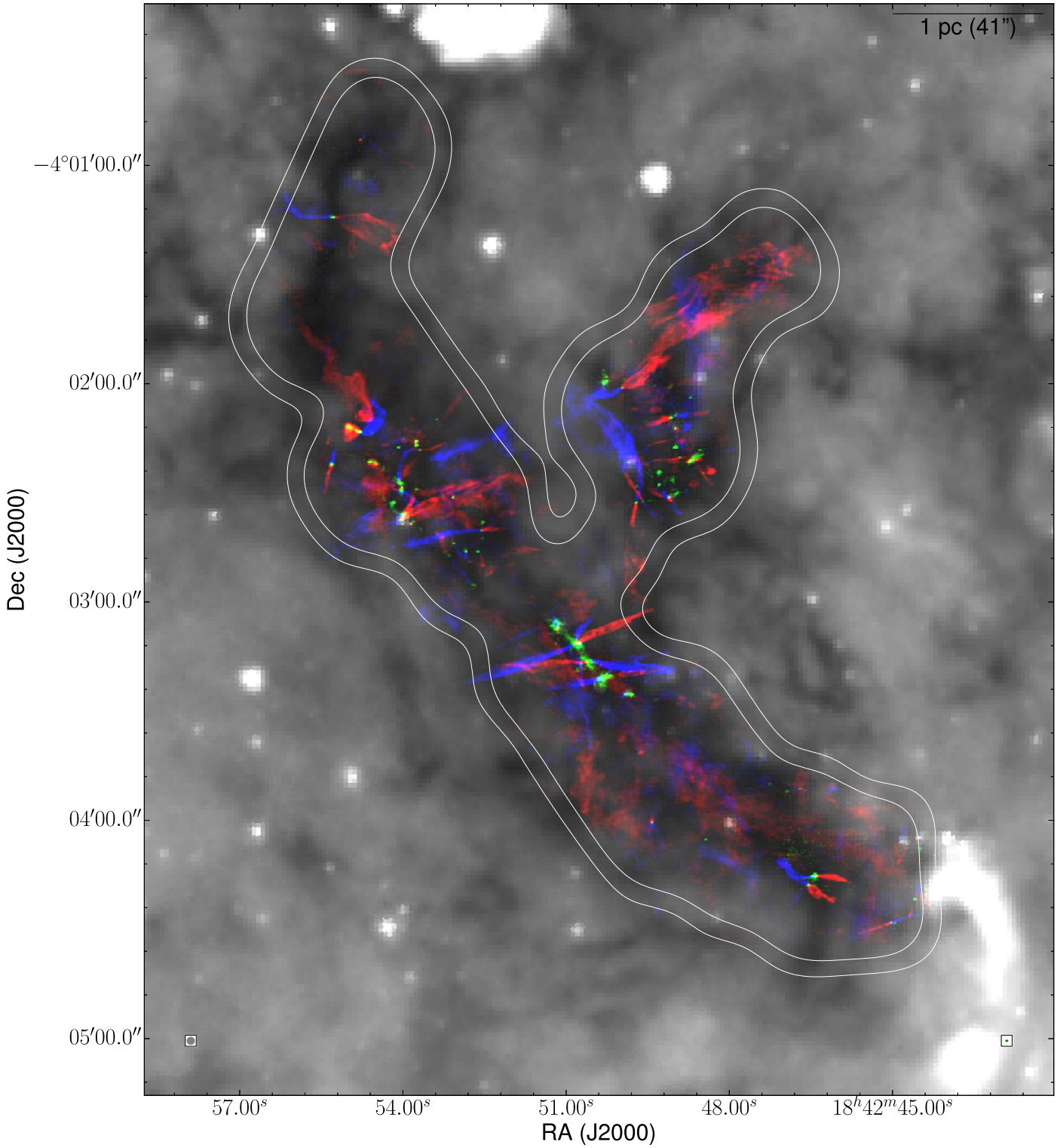

Figure 1. Map of molecular outflows in IRDC G28. Background grayscale image: *Spitzer* GLIMPSE 8 μm image (Benjamin et al. 2003; Churchwell et al. 2009). The resolution beam is shown as the gray circle at the lower left corner. Green: ALMA 1.3 mm continuum mosaic at 0.″5 resolution. The green ellipse at the lower right shows the ALMA synthesized beam. Red: redshifted CO(2-1) emission, integrated from 83.2 to 146.9 km s^{-1}. Blue: blueshifted CO(2-1) emission, integrated from 11.7 to 75.4 km s^{-1}. CO(2-1) maps have a similar spatial resolution to the continuum. The white contours show the ALMA primary-beam responses at 30% (outer) and 50% (inner). The top right scale bar shows a scale of 1 pc.

only studied continuum cores in the map that are within a primary-beam response >0.5 to ensure robust flux measurement. Here, we include continuum sources that are within a primary-beam response >0.2. A small number of continuum sources were not defined as cores in K19 because of their weak emission (below 4σ) or because of their small size (smaller than half beam size). However, in this paper, we include weak or small continuum sources ignored by K19, which are located at the center of a red and blue lobe pair or at the edge of a blue or red lobe, and thus appear to trace the dust surrounding a

Table 1
Outflows Properties

Source (1)	R.A. (2)	Decl. (3)	Blue PA (4)	Red PA (5)	PA_{Out} (6)	PA_{Fil} (7)	γ (8)
1	280.69353	−4.07084	93	−93	90	40	50
2_p1	280.71076	−4.05449	−96	93	88	49	39
2_p2	280.71076	−4.05449	107	−74	107	49	58
3	280.71328	−4.05201	14	−168	13	49	36
4	280.72522	−4.04092	⋯	−34	146	41	75
5	280.71186	−4.05317	109	−66	112	49	63
7	280.70419	−4.03817	−30	−180	165	12	27
8	280.70950	−4.03319	127	−51	128	38	90
9	280.72832	−4.03704	−102	73	75	158	83
10	280.72574	−4.04240	124	−76	114	46	68
11	280.71151	−4.05317	−178	–	2	49	47
12	280.70946	−4.05559	−30	146	148	49	81
13	280.72497	−4.04333	114	−65	115	46	69
15	280.70303	−4.03926	−88	93	92	126	34
19	280.73045	−4.03949	−10	163	166	45	59
21	280.70451	−4.03592	−83	105	101	12	89
22	280.73035	−4.02063	70	−111	69	5	64
23	280.70286	−4.03902	−175	14	10	126	64
33	280.69402	−4.07155	54	−125	55	40	15
35	280.70992	−4.05583	105	−81	102	49	53
37	280.72021	−4.04612	179	−1	179	133	46
38_p1	280.70465	−4.04199	80	−144	58	⋯	⋯
38_p2	280.70465	−4.04199	−148	65	48	⋯	⋯
40	280.72511	−4.04151	−121	79	69	5	64
41	280.68586	−4.07262	−17	164	163	⋯	⋯
44	280.72117	−4.04202	176	0	178	49	51
45	280.70717	−4.04238	−12	167	167	126	41
46	280.72534	−4.03817	108	⋯	108	51	57
48	280.70421	−4.03679	83	−99	82	12	70
49	280.72399	−4.04140	82	−95	83	174	89
54	280.69561	−4.06440	−89	96	93	60	33
56	280.70218	−4.03879	−80	98	99	126	27
58	280.72112	−4.04554	−148	28	30	101	71
60	280.70417	−4.03576	−86	93	94	12	82
61	280.71179	−4.05291	−18	⋯	162	49	67
62	280.71901	−4.04451	101	−79	101	10	89
63	280.72522	−4.04376	120	−56	122	46	76
65	280.70829	−4.03367	111	−55	118	38	80
66	280.70782	−4.03937	135	−66	125	⋯	⋯
71	280.72375	−4.03840	90	−89	91	174	83
75	280.70597	−4.06677	−174	3	4	120	64
76	280.72152	−4.04641	−142	25	32	160	52
79	280.70668	−4.04230	−145	32	33	126	87
82	280.68691	−4.06826	−15	171	168	⋯	⋯
84	280.68766	−4.07442	−73	107	107	70	37
85	280.71056	−4.05499	−79	102	102	49	53
94	280.72829	−4.01469	−43	156	146	137	9
106	280.72497	−4.03756	111	−69	111	51	60
107	280.69466	−4.06420	81	−100	81	60	21
109	280.71332	−4.05315	⋯	−149	31	49	18
134	280.72534	−4.04065	−6	−164	5	41	36
149	280.70270	−4.03879	45	−133	46	126	80
153	280.70616	−4.03994	109	−73	108	20	88
169	280.71381	−4.05161	115	−64	116	49	67
185	280.71992	−4.04694	87	−87	90	10	80
214	280.70783	−4.05676	151	⋯	151	68	83
237	280.69473	−4.06922	⋯	81	81	40	41
264	280.70258	−4.03981	⋯	−137	43	126	83
u1	280.72596	−4.01598	60	−115	63	60	3
u2	280.72757	−4.03604	−138	39	40	128	88
u3	280.70268	−4.03563	97	−82	97	12	85

Table 1
(Continued)

Source (1)	R.A. (2)	Decl. (3)	Blue PA (4)	Red PA (5)	PA_{Out} (6)	PA_{Fil} (7)	γ (8)
u4	280.70675	−4.03799	95	−81	97	43	54
u5	280.68556	−4.06795	−84	96	96	...	...
u6	280.70591	−4.03920	106	−82	102	20	82

Note. Columns 1–3 are introduced in Section 3.1. Columns 4–8 are defined in Section 3.3. Starting from column 2, all columns are in units of degrees.

protostellar outflow source. A total of six such sources, for which we include a "u" in their name, are identified. The names and coordinates of the continuum sources associated with outflows are listed in Table 1, columns 1–3.

Figure 2 shows the locations of the blue and redshifted lobes in our map with blue and red arrows, respectively. The arrows only indicate the position angle of the outflow axes and do not represent outflow sizes (all arrows have the same length). We note that our outflow catalog for G28 is likely incomplete. Although we have gone through the CO and SiO cubes to carefully search for outflows around continuum sources, we might still miss a few due to the complexity of the CO emission (especially in crowded regions). In particular, we would have likely missed small outflows that are within 5 km s^{-1} of the system velocity of 79.3 km s^{-1} (i.e., intrinsically low-velocity outflows or outflows that are approximately parallel to the plane-of-sky, yet buried in the complex cloud emission).

3.2. Filament Definition

To investigate the angle between the outflow axis and the parent filament, we define filamentary structures in G28. Note that we only focus on filaments that harbor outflow sources since our goal is to study the outflow-filament angle and not to conduct a comprehensive study of filaments in the IRDC. For this purpose, we use the 8 μm image from the *Spitzer* GLIMPSE survey (Benjamin et al. 2003; Churchwell et al. 2009). At this wavelength, the *Spitzer* image gives the best spatial resolution (2″, corresponding to ∼0.05 pc at a distance of 5 kpc) for tracing the high surface density filaments. We visually follow dark paths (i.e., filaments in absorption) in the cloud and overlay segments on top of the paths to define the filament spines (see Figure 2). Comparing with other techniques, we find the visual definition gives the most reliable results. In some of the regions, we also use dust continuum emission from our ALMA observations to help with the filament definition (see Figure 2(c)). The 1.3 mm ALMA continuum is particularly helpful for defining the filament axis on the plane of the sky in regions where infrared sources in the cloud break the dark path in the *Spitzer* mid-IR image. Note that the process of defining the filaments is independent from the process of identification of outflows.

Figure 2 shows how we defined the filament spines in G28. We zoom into five sub-regions (panels b-f correspond to the sub-regions "Neck", "Chest", "Claw", "Belly", and "Tail" in K19, respectively), each containing a group of protostellar continuum cores. In Figure 2, the arrows represent the position and orientation of outflow lobes. In most cases, the lines that define the filament cross the position of the protostellar cores that harbor the outflow sources. However, in a few cases, cores with outflows are at the border of filaments. In those cases, we associate the cores to the closest filament and calculate their relative PA. Five protostellar cores cannot be assigned to a nearby filament as they are relatively far away from a dark lane in the 8 μm image (indicated by square-circles in Figures 2(d) and (f)). These cores and their outflows are not included in the outflow-filament study.

3.3. Outflow PA Statistics

In total, 62 continuum sources are associated with at least one CO outflow lobe. Two continuum sources have double bipolar outflows. Four continuum sources have unipolar blueshifted outflows and four unipolar redshifted outflows. The rest of the 62 continuum sources have bipolar outflows. Hereafter, we follow the angle naming conventions in Stephens17: the position angle (PA) of the blueshifted lobe is referred to as "Blue PA"; that of the redshifted lobe is "Red PA"; the average outflow PA (see below) is denoted as "PA_{Out}"; the filament's PA is "PA_{Fil}"; the observed angle (projected on the plane of the sky) between PA_{Out} and the parent filament is "γ"; and the actual (three-dimensional; 3D) difference between the outflow and filament orientation (which is not directly observable) is denoted as γ_{3D} (see Section 3.3.2 for more details). Blue PA and Red PA are defined as the angle from north to east (counterclockwise on the sky), ranging from −180° to 180°. PA_{Out} and PA_{Fil} are also defined as the angle from north to east, but ranging from 0° to 180°. γ and γ_{3D} have values ranging from 0° to 90°. Blue PA, Red PA, PA_{Out}, PA_{Fil}, and γ for all the CO outflow lobes are shown in Table 1 columns 4–8, respectively.

3.3.1. Distribution of PA_{Out}

First, we investigate the distribution of PA_{Out}. A striking feature in Figure 1 is that a large number of the outflows seem to have an approximate east–west orientation. To confirm this, in Figure 3 panel (a), we plot the distribution of Blue PA and Red PA (shown in corresponding colors). It is clear that the histograms peak at ∼100° and ∼−80°, for Blue PA and Red PA, respectively, corresponding to the apparent east–west direction for most lobes mentioned above. We follow Stephens17 and derive the PA_{Out} by adding 180° to the outflow lobes with negative PA and averaging the Blue PA and Red PA for outflows with two lobes. For outflows with one lobe, we just use the orientation of that lobe as the PA_{Out} (adding 180° if negative). Figure 3(b) shows the distribution of PA_{Out} values. The histogram shows a peak at $PA_{Out} \sim 100°$, which is consistent with the visual examination of Figure 1, mentioned above. If the 3D orientation of outflows is random, then we would expect a uniform distribution of PA_{Out} in two dimensions. Following Stephens17, we carry out Anderson–Darling (AD) tests between the distribution of PA_{Out} and a uniform distribution. The p-value of the AD test is 0.15, indicating PA_{Out} is unlikely drawn from a uniform distribution. This suggests that the 3D outflow position angle is not randomly distributed.

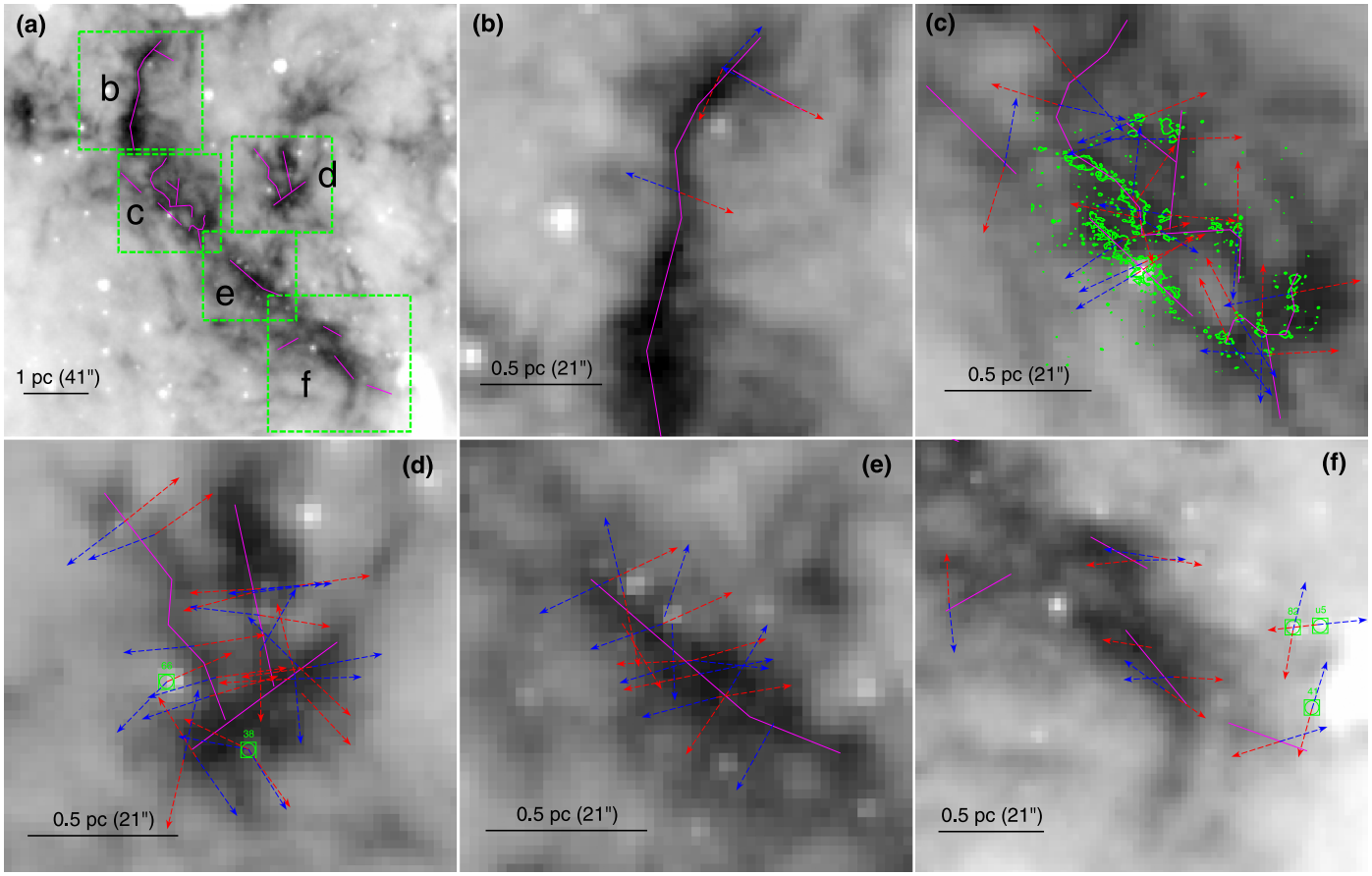

Figure 2. Summary of filaments and outflows. Panel (a) shows an overall view. The magenta segments show the visually defined filaments that pass through dark regions (high column density due to absorption; see Kong et al. 2018a). In panel (a), the (b)–(f) letters and the respective dashed rectangles represent the five sub-regions shown in panels (b)–(f). In panels (b)–(f) , corresponding to the five sub-regions ("Neck", "Chest", "Claw", "Belly", "Tail") defined in K19, the blue and redshifted outflow lobes are shown as blue and red dashed arrows, respectively. All arrows have the same length and do not represent the lobe lengths; only the position angle on the sky is meaningful. The green contours in panel (c) show the ALMA 1.3 mm continuum emission (contours represent 3, 4, 5σ, with σ being 0.08 mJy per 0.″5 beam). They are used to help define the filaments where infrared sources break the dark filament path. The box-circle symbol show the protostellar cores that cannot be associated with nearby filaments. They are not included in the outflow-filament analysis. A scale bar is included in each panel in the lower left corner.

3.3.2. *Outflow-filament Orientation*

Second, we investigate the relative orientation of the outflows with respect to their parent filament (γ_{3D}). Figure 3(c) shows the histograms of the observed angle between outflow lobes and their parent filament on the plane of the sky. Interestingly, the histograms show a higher number for PA $> 70°$ for both blue and redshifted outflow lobes. In fact, this is readily seen in Figure 2 where many arrows show large PA relative to the filaments. In Figure 3(d), we present the histogram of γ (i.e., the angle between PA_{Out} and PA_{Fil} on the plane of the sky). Again, following Stephens17, we calculate γ as

$$\gamma = \mathrm{MIN}\{|PA_{Out} - PA_{Fil}|, 180° - |PA_{Out} - PA_{Fil}|\}, \quad (1)$$

where γ is between 0° and 90° (see Equation (2) of Stephens17). In Figure 3(d), it is clear that there is a significantly higher number of outflows with angles with respect to their parent filament γ with values between 60° and 90° (32), compared to outflows with γ between 30° and 60° (19), and between 0° and 30° (7).

We emphasize that a large concentration of values of γ close to 90° does not necessarily mean that outflows tend to be perpendicular to the filaments in three dimensions. The measured values of γ (from our images) represent a projection of the actual 3D angle between outflow axes and their parent filament (γ_{3D}) on the plane of the sky. In other words, a value of $\gamma = 90°$ can be the projection on the plane of the sky of any γ_{3D} (see detailed discussions by Stephens17).

Here, we follow Stephens17 and carry out a Monte Carlo simulation that projects randomly generated γ_{3D} onto the plane of the sky to produce a distribution of values of γ, and compare them with our observations. The detailed methodology was described in Appendix A of Stephens17. Here, we briefly recap the process. We randomly generate N pairs of unit vectors with their 3D PA following the uniform distribution. Then, we calculate γ_{3D}, as the angle between the two unit vectors. Next, we project the two vectors onto the y–z plane and calculate their angle (equivalent to γ). Finally, we calculate the cumulative distribution function (CDF) of γ and compare with observations. We use $N = 10^6$ (the same as Stephens17) and reproduce their γ_{3D} CDF, shown in Figure 4(a) (compared with Figure 14 in Stephens17).

We also follow Stephens17 and consider three scenarios: (1) γ_{3D} with values only from 0° to 20°; (2) γ_{3D} with values only from 70° to 90°; (3) γ_{3D} with values from 0° to 90°. The first scenario corresponds to the "only parallel" case in Stephens17; the second the "only perpendicular" case; the third "completely

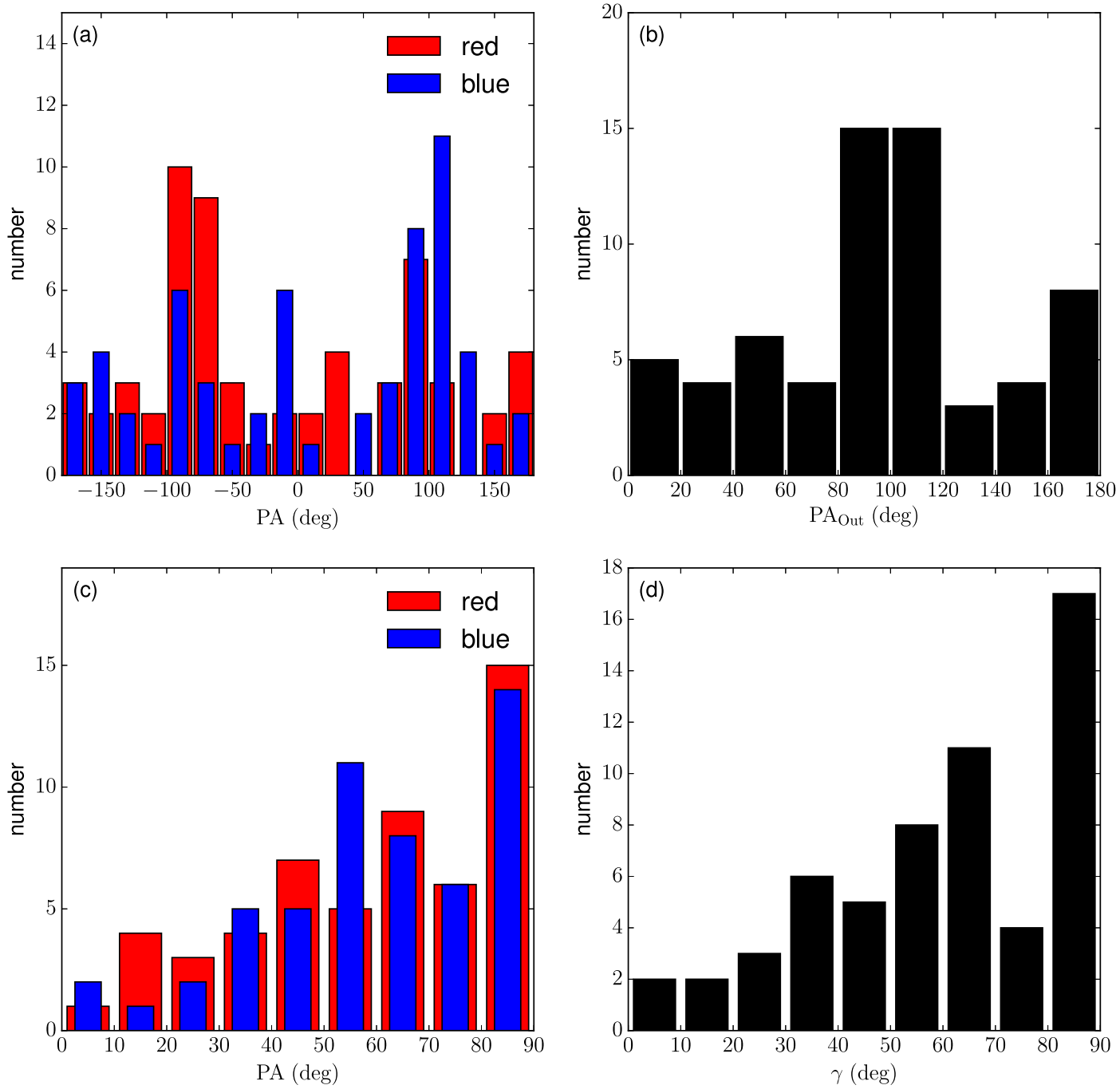

Figure 3. Outflow position angle distributions. (a) Position angle for blue and redshifted outflow lobes separately. The angle is between −180° and 180°. (b) Average position angle between blue and redshifted lobes, i.e., PA_{Out}. See Section 3.3. (c) Histograms for the observed angle between (blue and redshifted) lobes and filament orientation (PA_{Fil}). The angle is between 0° and 90°. (d) Histogram of γ (the angle between PA_{Out} and PA_{Fil}). See Section 3.3.

random." We plot the corresponding γ CDF for each of these three scenarios in Figure 4(b) (analogous to Figure 8 in Stephens17). It is immediately obvious that γ does not follow the "only parallel" scenario. Quite interestingly, the observed γ CDF appears to be consistent with the "only perpendicular" scenario. That is, in 3D space, outflows preferentially have axes that are approximately perpendicular to the orientation of their parent filaments, contrary to what was found in Perseus by Stephens17. A two-sample AD test between the observed γ CDF and simulated γ CDF for the "completely random" scenario (middle plot in Figure 4(b)) gives a *p*-value of 6.5×10^{-5}. It is therefore very unlikely that the underlying (3D) distribution of angles between outflows and filaments is completely random. On the other hand, a similar two-sample AD test comparing the observed γ with the simulated γ CDF for the "only perpendicular" scenario gives a *p*-value of 0.53, meaning that the hypothesis that the underlying angles between outflows and filaments are mostly perpendicular cannot be rejected. Given our results, we conclude that it is more likely that in G28, outflows are perpendicular to their parent filament rather than being parallel to, or having a random orientation with respect to, their parent filament.

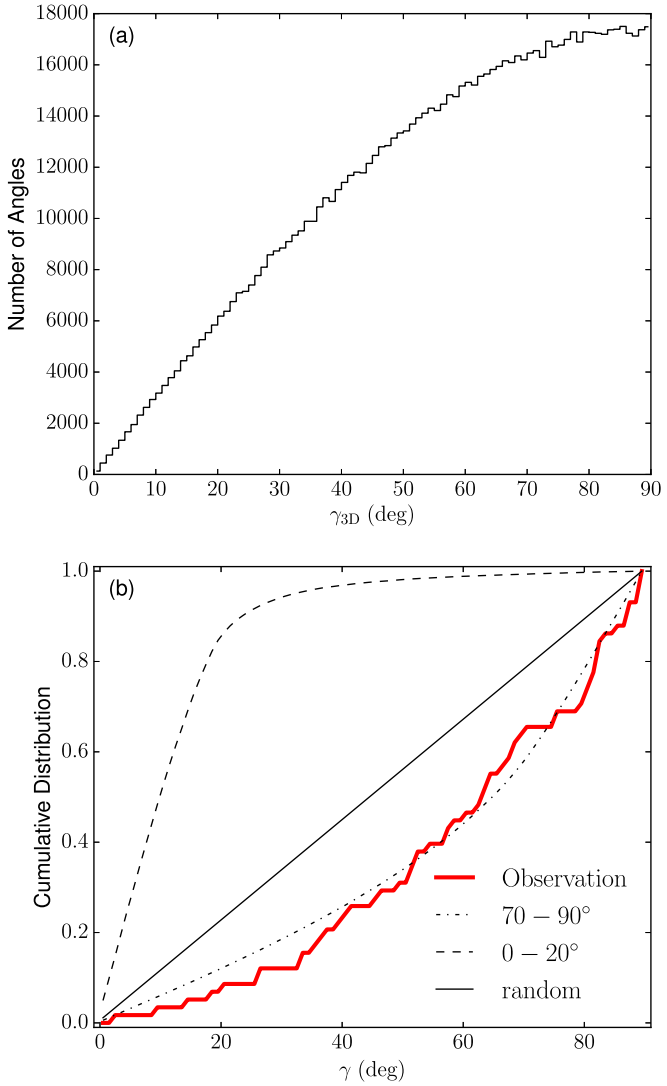

Figure 4. (a) CDF of the simulated γ_{3D}. See Section 3.3. (b) CDF of the two-dimensional γ based from the randomly generated γ_{3D}. Three scenarios are considered based on the distribution of γ_{3D}, i.e., "only parallel" (black dashed curve); "only perpendicular" (black dashed–dotted curve); "completely random" (black solid curve). The CDF of observed γ is plotted as a red curve. See Section 3.3 for additional details.

4. Discussion

The non-random outflow-filament angle in IRDC G28 suggests that the angular momentum of the protostellar accretion disk is correlated with the host filament. Then, two possible scenarios may explain this. In one scenario, the angular momentum direction is determined during the core fragmentation/formation and maintained for some time. In the other scenario, the angular momentum is a result of continuous mass accretion onto the core and then the accretion disk. Qualitatively, in the first scenario, the core is relatively isolated and no significant mass is deposited onto the core from the environment. In the second scenario, the core is constantly acquiring mass from its host filament.

Recently, Li et al. (2018) studied the formation of stellar clusters in a magnetized, filamentary IRDC, including early outflow feedback from the protostars. Since they were not able to resolve the disk formation scales, they adopted the direction of the net angular momentum at scales of several hundreds of astronomical unit as the outflow launching direction. Under these conditions, their results showed that outflows have a preferred orientation, which is perpendicular to the large-scale filament, as our observations suggest. In a follow-up paper, Li & Klein (2019) show that the outflow-filament angle is determined by the constant mass accretion from the filament to the embedded core, consistent with the second scenario stated above. These results highlight the importance of filament-core-disk accretion in SF. We note that in their simulation, a moderately strong magnetic field is used as an initial condition. Such dynamically important fields in IRDCs are reported by recent observations (e.g., Pillai et al. 2015). The filaments form perpendicular to the field, which results in the alignment of outflows with the direction of the original magnetic fields on the plane-of-the-sky. Following this result, our finding of the east–west outflow alignment in G28 (Section 3.3.1) may indicate that the magnetic field in this cloud has an east–west orientation. Future dust polarization measurements may confirm this.

Although we have not specifically studied the outflow size distribution, we note that their typical sizes based on Figure 1 are 0.1–1 pc. For an outflow lobe of 0.5 pc in length, and assuming a velocity of 100 $\mathrm{km\,s^{-1}}$ (the velocity of the driving jet, Bally 2016), the timescale is about 5000 yr. This implies that the outflow-filament alignment has been approximately stable for roughly the past few thousand years (except for those showing precession-like PA variations). It remains to be seen how long can the cloud maintain the filament-core-disk accretion that possibly gives rise to the outflow-filament alignment. Such an accretion process is important because it provides mass to the protostar from outside the core, thus having impact on the stellar IMF. More specifically, if the final stellar mass is dominated by the filament accretion, then the CMF–IMF relation would be questionable. On the other hand, if the filament accretion is limited, then it is possible that there might be a statistically significant relation between the CMF and the IMF.

Several observational studies have shown that the direction of the angular momentum at core/disk scales is not correlated with the filamentary structure (Davis et al. 2009; Tatematsu et al. 2016, Stephens17). Possible causes are protostellar multiplicity (Lee et al. 2016; Offner et al. 2016), and/or an underlying bimodal distribution, with one sub-population of outflow directions that is preferentially parallel and another that is perpendicular to filaments (Stephens17). It would be useful to carefully examine any differences between the clouds to investigate whether differences in outflow-filament alignment is caused by the cloud environment or evolutionary stage.

5. Summary and Conclusions

In this paper, we have investigated the distribution of outflow position angles in the IRDC G28.37+0.07. We have defined molecular outflows in the CO(2-1) cube observed with ALMA. In total, we have identified CO outflows from 62 1.3 mm continuum cores. Fifty-four cores have bipolar outflows and two of them show double bipolar outflows. Four cores have blueshifted unipolar outflows and four have redshifted unipolar outflows. We have studied the statistics of the (CO) outflow position angles. In particular, we have found that the outflow position angles in G28.37+0.07 are not randomly oriented. Albeit spread over the extent of the dark cloud, the plane-of-sky outflows preferentially align at a position angle of ~100°, roughly corresponding to an east–west direction.

We have visually defined filamentary structures along the dark paths in the *Spitzer* 8 μm near-infrared image. The dark paths correspond to high-mass surface density filamentary structures. At the location of each protostellar core that drives an outflow, we have measured the filament position angle and compared it with the position angle of the outflow. In G28.37 +0.07, we have observed a higher number of continuum sources with an observed (projected on the plane of the sky) angle between the outflow axis and the parent filament close to 90°. We have carried out Monte Carlo simulations of the 3D orientation between the outflow and filament and projected it onto two dimensions to mimic plane-of-the-sky observations. A comparison of the CDFs of the observed and simulated plane-of-sky outflow-filament angles shows that outflows are preferentially perpendicular to filaments.

This finding is consistent with recent numerical work (Li et al. 2018), which supports the physical picture that protostellar accretion is fed by gas flow along filaments in IRDCs, highlighting the importance of filamentary structures in SF. On the other hand, studies in, e.g., the Perseus cloud (Stephens et al. 2017), have not shown such alignments. We now need to understand whether these two seemingly contrasting results indicate that there are two intrinsically different modes of SF or this is merely an evolutionary effect. Since G28.37+0.07 is massive, infrared dark, and probably forming the first-generation stars, it provides an excellent archetype to be compared with other well-known star-forming clouds at different evolutionary stages.

We thank the anonymous referred for helpful comments. We thank Pak Shing Li for fruitful discussions. S.K. and H.G.A. were funded by NSF award AST-1140063 and AST-1714710 while conducting this study. This paper makes use of the following ALMA data: ADS/JAO.ALMA#2013.1.00183.S and ADS/JAO.ALMA#2015.1.00183.S. ALMA is a partnership of ESO (representing its member states), NSF (USA) and NINS (Japan), together with NRC (Canada), NSC and ASIAA (Taiwan), and KASI (Republic of Korea), in cooperation with the Republic of Chile. The Joint ALMA Observatory is operated by ESO, AUI/NRAO and NAOJ. The National Radio Astronomy Observatory is a facility of the National Science Foundation operated under cooperative agreement by Associated Universities, Inc. This work is based [in part] on observations made with the *Spitzer Space Telescope*, which is operated by the Jet Propulsion Laboratory, California Institute of Technology under a contract with NASA.

Facilities: ALMA, *Spitzer*.

Software: Astropy (Astropy Collaboration et al. 2013), Numpy (van der Walt et al. 2011), APLpy (Robitaille & Bressert 2012), Matplotlib (Hunter 2007), Glue (Beaumont et al. 2015; Robitaille et al. 2017), SAOImageDS9 (Joye & Mandel 2003).

ORCID iDs

Shuo Kong https://orcid.org/0000-0002-8469-2029
Héctor G. Arce https://orcid.org/0000-0001-5653-7817
María José Maureira https://orcid.org/0000-0002-7026-8163
Paola Caselli https://orcid.org/0000-0003-1481-7911
Jonathan C. Tan https://orcid.org/0000-0002-3389-9142
Francesco Fontani https://orcid.org/0000-0003-0348-3418

References

André, P., Di Francesco, J., Ward-Thompson, D., et al. 2014, in Protostars and Planets VI, ed. H. Beuther et al. (Tucson, AZ: Univ. Arizona Press), 27
Arce, H. G., Shepherd, D., Gueth, F., et al. 2007, in Protostars and Planets V, ed. B. Reipurth, D. Jewitt, & K. Keil (Tucson, AZ: Univ. Arizona Press), 245
Astropy Collaboration, Robitaille, T. P., Tollerud, E. J., et al. 2013, A&A, 558, A33
Bally, J. 2016, ARA&A, 54, 491
Beaumont, C., Goodman, A., & Greenfield, P. 2015, in ASP Conf. Ser. 495, Astronomical Data Analysis Software an Systems XXIV (ADASS XXIV), ed. A. R. Taylor & E. Rosolowsky (San Francisco, CA: ASP), 101
Benjamin, R. A., Churchwell, E., Babler, B. L., et al. 2003, PASP, 115, 953
Butler, M. J., Tan, J. C., & Kainulainen, J. 2014, ApJL, 782, L30
Carey, S. J., Feldman, P. A., Redman, R. O., et al. 2000, ApJL, 543, L157
Chabrier, G., & Hennebelle, P. 2010, ApJL, 725, L79
Churchwell, E., Babler, B. L., Meade, M. R., et al. 2009, PASP, 121, 213
Cosentino, G., Jiménez-Serra, I., Henshaw, J. D., et al. 2018, MNRAS, 474, 3760
Davis, C. J., Froebrich, D., Stanke, T., et al. 2009, A&A, 496, 153
Duarte-Cabral, A., Bontemps, S., Motte, F., et al. 2013, A&A, 558, A125
Fernández-López, M., Arce, H. G., Looney, L., et al. 2014, ApJL, 790, L19
Fielding, D. B., McKee, C. F., Socrates, A., Cunningham, A. J., & Klein, R. I. 2015, MNRAS, 450, 3306
Frank, A., Ray, T. P., Cabrit, S., et al. 2014, in Protostars and Planets VI, ed. H. Beuther et al. (Tucson, AZ: Univ. Arizona Press), 451
Hopkins, P. F. 2012, MNRAS, 423, 2037
Hunter, J. D. 2007, CSE, 9, 90
Joye, W. A., & Mandel, E. 2003, in ASP Conf. Ser. 295, Astronomical Data Analysis Software and Systems XII, ed. H. E. Payne, R. I. Jedrzejewski, & R. N. Hook (San Francisco, CA: ASP), 489
Kirk, H., Myers, P. C., Bourke, T. L., et al. 2013, ApJ, 766, 115
Kong, S. 2019, ApJ, 873, 31
Kong, S., Tan, J. C., Arce, H. G., et al. 2018a, ApJL, 855, L25
Kong, S., Tan, J. C., Caselli, P., et al. 2016, ApJ, 821, 94
Kong, S., Tan, J. C., Caselli, P., et al. 2017, ApJ, 834, 193
Kong, S., Tan, J. C., Caselli, P., et al. 2018b, ApJ, 867, 94
Lee, K. I., Dunham, M. M., Myers, P. C., et al. 2016, ApJL, 820, L2
Li, P. S., & Klein, R. I. 2019, arXiv:1901.04593
Li, P. S., Klein, R. I., & McKee, C. F. 2018, MNRAS, 473, 4220
Lim, W., Tan, J. C., Kainulainen, J., Ma, B., & Butler, M. J. 2016, ApJL, 829, L19
McKee, C. F., & Ostriker, E. C. 2007, ARA&A, 45, 565
Motte, F., Bontemps, S., & Louvet, F. 2018, ARA&A, 56, 41
Offner, S. S. R., Dunham, M. M., Lee, K. I., Arce, H. G., & Fielding, D. B. 2016, ApJL, 827, L11
Peretto, N., Fuller, G. A., André, P., et al. 2014, A&A, 561, A83
Pillai, T., Kauffmann, J., Tan, J. C., et al. 2015, ApJ, 799, 74
Pillai, T., Wyrowski, F., Carey, S. J., & Menten, K. M. 2006, A&A, 450, 569
Ragan, S., Henning, T., Krause, O., et al. 2012, A&A, 547, A49
Robitaille, T., Beaumont, C., Qian, P., Borkin, M., & Goodman, A. 2017, multidimensional data exploration glueviz: multidimensional data exploration, v0.13.1, Zenodo, doi:10.5281/zenodo.1237692
Robitaille, T., & Bressert, E. 2012, APLpy: Astronomical Plotting Library in Python, Astrophysics Source Code Library, ascl:1208.017
Sanhueza, P., Jackson, J. M., Zhang, Q., et al. 2017, ApJ, 841, 97
Schneider, N., Csengeri, T., Klessen, R. S., et al. 2015, A&A, 578, A29
Shu, F. H., Adams, F. C., & Lizano, S. 1987, ARA&A, 25, 23
Simon, R., Jackson, J. M., Rathborne, J. M., & Chambers, E. T. 2006, ApJ, 639, 227
Stephens, I. W., Dunham, M. M., Myers, P. C., et al. 2017, ApJ, 846, 16
Tan, J. C., Beltrán, M. T., Caselli, P., et al. 2014, in Protostars and Planets VI, ed. H. Beuther et al. (Tucson, AZ: Univ. Arizona Press), 149
Tan, J. C., Kong, S., Butler, M. J., Caselli, P., & Fontani, F. 2013, ApJ, 779, 96
Tan, J. C., Kong, S., Zhang, Y., et al. 2016, ApJL, 821, L3
Tatematsu, K., Ohashi, S., Sanhueza, P., et al. 2016, PASJ, 68, 24
van der Walt, S., Colbert, S. C., & Varoquaux, G. 2011, CSE, 13, 22
Wang, K., Zhang, Q., Testi, L., et al. 2014, MNRAS, 439, 3275
Wang, K., Zhang, Q., Wu, Y., Li, H.-b., & Zhang, H. 2012, ApJL, 745, L30
Wang, K., Zhang, Q., Wu, Y., & Zhang, H. 2011, ApJ, 735, 64
Wang, Y., Zhang, Q., Pillai, T., Wyrowski, F., & Wu, Y. 2008, ApJL, 672, L33
Zhang, Q., Wang, K., Lu, X., & Jiménez-Serra, I. 2015, ApJ, 804, 141
Zhang, Q., Wang, Y., Pillai, T., & Rathborne, J. 2009, ApJ, 696, 268
Zinnecker, H., & Yorke, H. W. 2007, ARA&A, 45, 481